

Emergent false vacuum decay processes in a two-dimensional electronic crystal: experiment vs. simulations on a noisy superconducting quantum processor

Jaka Vodeb^{*1,2,3}, Michele Diego¹, Yevhenii Vaskivskyi¹, Leonard Logaric¹, Yaroslav Gerasimenko¹, Viktor Kabanov¹, Benjamin Lipovsek⁴, Marko Topic⁴ and Dragan Mihailovic^{*1,2,5}

¹*Jozef Stefan Institute, Jamova 39, 1000 Ljubljana, Slovenia*

²*Faculty of Mathematics and Physics, University of Ljubljana, Jadranska 19, Ljubljana, Slovenia*

³*Institute for Advanced Simulation, Jülich Supercomputing Centre, Forschungszentrum Jülich, Wilhelm-Johnen-Straße, 52425 Jülich, Germany*

⁴*Faculty for Electrical Engineering, University of Ljubljana, Tržaška 25, 1000 Ljubljana, Slovenia*

⁵*CENN Nanocenter, Jamova 39, 1000 Ljubljana, Slovenia*

*jaka.vodeb@ijs.si, *dragan.mihailovic@ijs.si

Emergent metastability in non-equilibrium systems is a subject that touches everything from the origins of life¹ to the quantum nature of the universe². In condensed quantum matter, a good topical example is the metastability of topologically inhibited self-organization of electronic domains in a correlated electronic crystal in the aftermath of a symmetry-breaking phase transition³. Understanding the dynamics of such systems is crucial for developing new quantum technologies and exploring fundamental aspects of many-body non-equilibrium quantum mechanics. Here, a non-equilibrium state is set up by carrier injection in the quantum material (M), resulting in a domain structure, whose time-evolution is investigated by scanning tunneling microscopy. Demonstrating a new approach to modelling of emergent non-equilibrium quantum behavior, we use an array of 2008 qubits in a programmable noisy superconducting quantum simulator (NSQS) without error correction (P), in which mutual qubit interconnections correspond directly to the electronic interactions on the triangular lattice of the electronic crystal material. The success of the simulations critically depends on both the faithfulness of the model correspondence between the two systems and careful management of the decoherence pathways. Importantly, decoherence of both P and M is driven by noise with a characteristic $1/\nu$ frequency spectrum. The simulations reveal how an emergent false vacuum state arises, describing the time evolution and temperature dependence of the observed electronic domain dynamics of M solely on the basis of microscopic electronic interactions. The parallel experiments demonstrate the potential of NSQSs for studying emergent non-equilibrium dynamics in complex many-body quantum systems.

Many-body systems emerging through symmetry-breaking phase transitions typically end up in an inhomogeneous intermediate state before reaching a homogeneous ground state. In the aftermath of second-order transitions, such as the superconducting transition in type-2 superconductors, fluctuations in the phase ϕ of the order parameter force causally unconnected regions to evolve independently, forming mesoscopic vortex structures^{4–6}. In the aftermath of first-order phase transitions, the dynamics involves nucleation of the new phase, followed by coalescence⁷ and “ripening”⁸. Topological and jamming transitions present even more complex non-equilibrium dynamics^{9,10}. In classical systems, this kinetics is primarily diffusion-driven, while in quantum systems¹¹, we may additionally expect to observe direct incoherent macroscopic tunneling (IMT) and noise-assisted processes between different mesoscopic state configurations, particularly at low temperatures¹². Microscopic interactions in the resulting state lead to self-assembly of its constituents and the emergence of complex new mesoscopic states. The resulting metastable states exhibit complex emergent dynamics that are observed in various fields, from nucleosynthesis¹³ to non-equilibrium superconductivity¹⁴.

The experimental challenge is to measure the reconfigurations of the many-body system in order to unambiguously identify mesoscopic tunneling processes, and measure the dynamics. Because such processes are common, and have important potential applications¹⁵, the ability to faithfully simulate their dynamics on a quantum level would lead to significant progress in understanding metastable states in quantum materials and non-equilibrium quantum devices. In electronic crystals, the ordering of domains and discommensurations are traditionally modelled classically by an anisotropic Ising model with competing interactions¹⁶, or by continuum models^{17,18} but these models give little insight into how inhomogeneities evolve. Ab-initio methods can give detailed electronic band structure information of individual domain walls¹⁹, but cannot be used to simulate the emergent many-body collective dynamics.

Quantum simulations of ground state properties in many body systems, as well as metastable decay of complex systems using ultracold atomic lattices have recently been demonstrated^{20,21}, and the majority of recent attention has focused on noisy intermediate scale quantum (NISQ) processors, but extension to real-world non-equilibrium systems, such as is addressed here, is particularly challenging because it requires control of decoherence and hence control of the coupling to the environment. Here, using a new approach, both the natural material M and the simulation P that are investigated in parallel along the principles of simulating nature with nature²². The two systems have inherently similar decoherence mechanisms. The presented simulation leads to remarkable insights into how microscopic

many-body interactions between electrons on a superlattice conspire to display metastable quantum domain dynamics observed in experiments.

Our experimental system (M) is the prototype quasi-two-dimensional (2D) strongly correlated transition metal dichalcogenide material 1T-TaS₂²³. Because of a strong electron-phonon interaction in this material, the electronic kinetic energy K is exponentially reduced²⁴, and Coulomb energy V becomes dominant²⁵. This means that the essential physics in this regime comes from the formation of mutually repulsive heavily dressed quasiparticles – polarons²⁶, and leads to a variety of ordered charge density wave states with metastable domain structures^{26–28} (Fig.1a,b and the material is described in more detail in the SI). In response to external perturbation, 1T-TaS₂ displays metastable states associated with the formation of domains in the low-temperature electronic superlattice whose temporal reconfigurations can be observed in detail by scanning tunneling microscopy (STM). The classical many-body relaxation dynamics of such domain states is topologically inhibited^{29,30}, leading to the formation of an effective energy barrier for the transition between different domain configurations, requiring a topological transition, or a global symmetry-breaking phase transition to reach the ground state. When topology and low temperatures inhibit classical dynamics, the quantum tunneling processes that can cause relaxation of the false vacuum state to the ground state is a topic of wide interest.

Domain Reconfiguration Measurements

In the present experiments, a metastable domain state in 1T-TaS₂ is set up at 4 K by an electrical pulse charge injection through an STM tip^{29,31,32}. As the domain structure evolves in time, its configuration is recorded periodically by STM (Fig.1c), whereby the tip is retracted and set to zero bias between measurements to avoid reconfiguration by spurious signals from the tip. This measurement results in classical sequential “snapshots” of the domain configurations (see SI for experimental details). The reconfigurations between sequential images are quantified by measuring the Hamming distance, defined as the number of altered occupied positions between frames (Fig.1c), expressed as the fraction of polarons moved $f = \Delta N/N$, where N is the total number of charges per frame (Fig.1d). Characteristically, jumps of f appear with time (Fig.1d), reflecting the discrete nature of domain reconfiguration³³. $f(t)$ averaged over a large number of scans on different areas of the sample at 5 K shows an approximately exponential decay. As expected, at 4 K the classical power law time dependencies $f(t) \sim r(t)^2 \sim t^{-1}$ or $t^{-2/3}$, that would be characteristic of nucleation and coalescence processes⁷ at higher temperatures³⁴, do not fit the data (see Fig.1e). A crucial test of the experiments is to see if, and how, the STM tip influences the reconfiguration process. Comparing $f(t)$ obtained by

tip scanning at regular intervals (Fig.1e), with $f(t)$ measured under identical experimental conditions, but with a retracted tip, we see in Fig.1f that the two have very similar $\tau = 1040 \pm 90$ s and 945 ± 80 s respectively, implying that the influence of the STM tip is negligible, within experimental error. A number of other tests that support this conclusion are given in the supplement, including a detailed calculation of Joule heating by the STM tip current. Having established that the noise in M does not originate from the STM tip, other possible excitation sources are acoustic phonons, charge fluctuations in the substrate and at the interface, as well as spurious electro-magnetic fields. Importantly for our purposes, in 1T-TaS₂ the noise has been experimentally measured to have a $\sim 1/\nu$, frequency dependence, which will be relevant in our simulations.³⁵

The dependence of the reconfiguration rate on sample temperature in system M is shown in Fig. 1g. The rate exhibits a crossover from T -independent to T -dependent behavior at a temperature $T_0 \approx 20$ K. The data can be fit to: $R(T) = R_q + R_0 \exp(-E_M/k_B T)$, where $R_q \simeq 8 \pm 1 \times 10^{-4}$ s⁻¹ is the T -independent tunneling rate, and the second term describes T -activated hopping across a barrier. The value $E_M = 6 \pm 3$ meV obtained from the fit to the data in Fig. 1g is of the same order as the activation energy $E_A = 10 \sim 20$ meV obtained from thermally activated macroscopic resistance relaxation measurements³³, providing an important experimental consistency check. Since by STM we observe “snapshots”, effectively separated by large time windows, we assume that reconfigurations correspond to single escape events from a local minimum in the energy landscape. The free energy landscape E for the system as a function f is shown schematically in the insert to Fig.1d. Different minima in $E(f)$ correspond to different configurational states, while the excited states within the wells correspond to configurations which conserve f , such as translations. We emphasize that E is a complex 2^N dimensional function of all possible configurations and f only measures the distance that M travels through configurational space between subsequent events. There are multiple possible paths for M to take, either thermally across a barrier or via quantum tunneling, in order to travel the same distance f from a specific starting configuration. However, it is safe to assume that there exists a most likely path, which will minimize the action of the Hamiltonian governing the dynamics, meaning that we can locally approximate the energy landscape with a cubic potential.

The measured $f(t)$ is related, within a scaling factor, to the canonical Kramers-Caldeira-Leggett (KCL) quantum decay rate³⁶ of a system moving through a cubic potential in a 1D configurational landscape (Fig. 2b). Initially, M is trapped in a metastable minimum, oscillating with a frequency ω_0 determined by the minimum’s curvature in the harmonic approximation. $\hbar\omega_0$ is also approximately the average level spacing of the many-body energy spectrum describing M. The cubic potential exhibits a

barrier, which M has to overcome, either by quantum tunneling or thermal activation. KCL theory predicts a crossover temperature T_0 from thermally activated to quantum mediated escape within a range ΔT . If we take the experimental values E_M , $T_0 = 20\text{ K}$ and $\Delta T = 10\text{ K}$, obtained from Fig. 1g and plug them into KCL theory, it predicts $\frac{E_M}{\hbar\omega_0} \simeq 0.4 \sim 1.4$. This is in direct contradiction with the underlying assumptions of KCL theory $\frac{E_M}{\hbar\omega_0} \gg 1$, which renders it unapplicable in our case. A comprehensive extension of the theory into the regime $E_M \sim \hbar\omega_0$ would be required, which does not currently exist. For this reason the present direct programmable simulation of M with P is valuable, because it allows us to probe parameter regimes currently unavailable through analytical and numerical approaches. Nevertheless, KCL analysis does suggest that the energy scale responsible for dynamics of M is comparable to E_M . As a sanity check, we also performed classical Monte Carlo simulations, which predict a quantum rate > 0 only for unphysical microscopic processes (see SI for details) and are therefore also inconsistent with observations in M. On the other hand, a simple WKB estimate of the macroscopic tunneling rate given in the supplement suggests that the observed reconfiguration timescale is plausible with reasonable parameters.

Simulation of Domain Reconfiguration Dynamics

To simulate the dynamics, P is implemented directly on D-Wave's Advantage_system6.1 (the NSQS). The microscopic interaction between polarons on the triangular lattice of M is geometrically mapped onto the coupling between physical qubits (Fig. 2a). A custom embedding scheme maps physical to logical qubits while minimizing the required overhead of physical qubits. The couplings were chosen to be native to P in order to mitigate systematic errors³⁷. Here we describe the salient features of the calculation, while the embedding, detailed theoretical model, its justification, and discussion of the noise on simulations are described in detail in the SI. Importantly, the noise characteristics of P have been extensively studied on a phenomenological level, and the qubits in P are known to be subjected to flux and charge noise with a $1/\nu$ frequency spectrum³⁸. Although a concrete microscopic mechanism for flux noise in P is still missing, the two most likely sources are randomly oriented electronic spins at the metal-oxide interface and defects in dielectrics. While the noise may have different microscopic origins, qubits in system P are subject to decoherence due to external influence in much the same way as the electronic states in the physical crystal M. We combine this with the fact that P and M both have $1/\nu$ noise spectra and thereby justify the quantitative comparison of the two systems' dynamics. We capture this equivalence between M and P with the assumption that both systems are described by the Hamiltonian $H = H_S + H_I + H_B$, where H_S represents the system of polarons we observe in M, which are mapped onto P. The noise is introduced as an external bath H_B , which is coupled to the system via

H_I and its effect is a static energy shift of the energy levels of H_S . If H_B is a two-level system, neighboring energy levels of H_S will split into 4 and the gap is reduced by $\sim W$. As the number of coupled two-level systems increases, the 2 levels become bands of width W , determined entirely by the noise spectrum, as shown in Fig. 2b. If the energy bands overlap, then a transition between the bath degrees of freedom can already induce a polaronic configurational change. If they do not overlap, the bare tunneling gap is still reduced by W , increasing the probability for a transition. Both represent incoherent macroscopic tunneling (IMT) processes.

We now make the correspondence between M and P more explicit. We describe M with a single band tight-binding microscopic Hamiltonian H_M , including phonon degrees of freedom via the Fröhlich interaction, and a long-range Coulomb repulsion $V_c(i,j)$ between electrons. Such a model exhibits polarons as quasiparticles, which repel each other, and exhibit an exponentially suppressed tunneling matrix element²⁴. We neglect the spin degree of freedom and attribute to each atomic site a binary variable $q_i \in \{0,1\}$ (a qubit), which represents the polaron occupancy of the site. It also follows that the quantity $f(t) = \Delta N/N$ measured in experiments is the normalized Hamming distance between different configurations, where now the Hamming distance is the number of changed q_i between different configurations. Next, we map H_M the onto the transverse field Ising model (TFIM) $H_S = -A(s) \sum_i \sigma_i^x / 2 + B(s) (\sum_{i < j} J_{i,j} \sigma_i^z \sigma_j^z + \sum_i h_i \sigma_i^z) / 2 = A(s) H_x + B(s) H_z$, where $\sigma_i^{x,z}$ are Pauli matrices operating on q_i , $J_{i,j}$ are couplings between qubits q_i and q_j , h_i is the longitudinal external field exerted upon q_i and $s(t)$ is a custom time dependent function ranging from 0 to 1 that controls the annealing schedule. We simulate H on P at different temperatures T by adjusting the ratio $H/k_B T$, where $H_S/k_B T = (-H_x + r H_z)/T_{eff}$, where $T_{eff} = k_B T/A(s)$, $r = J B(s)/A(s)$ and J a dimensionless tunable parameter on P which sets the magnitude of H_z , which represents the potential energy of polarons and is limited to nearest neighbor repulsion with a magnitude of 1, while the diagonal elements represent the chemical potential and are set to -1 . H_x represents the kinetic energy of polarons. The parameter r represents the scale of the potential and kinetic energy ratio. 1T-TaS₂ is expected to have $r \gg 1$, which is confirmed by our simulations. T_{eff} measures the dimensionless ratio of the temperature energy scale to the Hamiltonian's interaction scale. The physical temperature of P is fixed to $T_P = 16 \pm 0.1 \text{ mK}$, which means that we can only adjust T_{eff} by adjusting the interaction scale $A(s)$. The values of T_{eff} and r are set by using a customizable annealing schedule feature $s(t)$, which determines the value of $A(s)$ and $B(s)$ according to Ref.³⁹. $s(t)$ was chosen to be a linear ramp down from 1, in a time $t_a/2$, to the value specified by the parameters T_{eff} and r , and then back up to

1 in a time $t_a/2$. t_a is chosen to be $5 \sim 10 \mu s$, which is sufficient to ensure incoherent relaxation towards thermal equilibrium.

As expected, the simulations give the ground state of H_z to be an ordered triangular polaronic superlattice with 1 polaron per 3 atomic lattice sites with 3 possible superlattices, each displaced by one site along the atomic lattice vectors (Fig. 2c). A solid-gas transition temperature, which is analogous to the paramagnetic to anti-ferromagnetic transition in the TFIM, depends approximately linearly on r as $T_{eff}^c = 0.55 r + 0.22$ ($\pm 5\%$), extracted from a fit to the phase diagram shown in Fig. 2e. If our chosen initial state is a domain state, we observe similar domain wall dynamics in our simulated system P as in system M, where domains reconfigure towards the uniform ground state. Fig. 2d shows a typical relaxation sequence from an initial domain state, obtained from relaxation on P from a high-energy fully occupied state, in order to be the equivalent of Fig. 1c in system M. Figs. 2f and 2g show the calculated $f(t)$ and $R(T_{eff})$ respectively, which can be compared with the experimental Figs. 1d and 1g. At high T_{eff} , $R(T_{eff})$ eventually saturates (not shown), as the system approaches the gas phase. Focusing on low- T relaxation dynamics, we see that at low T_{eff} , $R(T_{eff})$ saturates due to ordering of the system into the ground state. However, the rate remains finite as the relaxation rate becomes slow compared to our sampling rate, so the system has not had time to fully order.

The simulations give us some unique insights into the emergent tunneling phenomenon. The dynamics of the two systems is governed by an anharmonic metastable state potential in terms of the configurational coordinate, measured by Hamming distance f , for M and P respectively. While the washboard potential and two-level system dynamics of flux qubits in the P are determined by the device concept, the energy landscape of the metastable state of M is determined by the topology and the microscopic details of the domain structure arising from discommensurations¹⁹.

The extracted parameters from the simulations describing the emergent processes are the barrier energy E_B (height) and the barrier width w which describe the rate of tunneling between domain configurations. In M, the thermal activation energy E_B is determined directly from the T -dependence of the rate in Fig. 1c or resistivity relaxation to be $E_M \simeq 10 \sim 20 \text{ meV}$. On the other hand, w is related to the Hamming distance f , where both are measured in terms of the configurational coordinate, which is set by the state of N Bloch spheres representing qubits, parametrized by $2N$ spherical angles. The plot of $f(t)$ in Fig. 1d thus reflects the tunnel barrier width for each measured reconfiguration. The value of the simulations is to describe this behavior on the basis of microscopic inter-particle interaction with only r as the adjustable parameter. The energy landscape of M is reproduced with an appropriately

scaled Hamiltonian H , which guides the system from an initial non-equilibrium state towards thermal equilibrium in the presence of a $1/\nu$ noise spectrum. The quantum domain dynamics introduced by the tunneling term in the TFIM exhibits the same timescale ~ 1000 s in P as in M for $r \approx 58$, given by the extrapolation of an exponential fit from data obtained with P, without any adjustment for the difference in energy scales between P and M.

Conclusions

Incorporating external noise in programmable simulations of real-world experiments, rather than trying to eliminate it with error correction algorithms, is shown to give a remarkably insightful description of non-equilibrium phenomena in a quantum material. The emergent many-body dynamics is simulated solely on the basis of microscopic interactions with a single effective adjustable parameter r which tunes the ‘quantum-ness’ of the system. On the basis of modeling, we can ascertain the appropriate timescale of quantum decay dynamics in 1T-TaS₂ and the bare tunneling gap responsible for false vacuum decay. The simulations clearly display a crossover from T -activated dynamics to T -independent quantum domain melting that is experimentally observed in the STM measurements, and give remarkable insight into the mechanism for the emergence of false vacuum states in a microscopic system. This demonstrates the usefulness of noisy quantum modeling for simulating emergent non-equilibrium many-body dynamics of mesoscopic inhomogeneities with only fundamental inter-particle interactions, which is relevant in a wide variety of non-equilibrium quantum systems – including quantum materials such as the quantum paraelectric SrTiO₃⁴⁰, or tunneling between false vacuum states that emerge from elementary interactions in the early cosmological energy landscape^{41–43}. Apart from fundamental interest, modeling quantum reconfiguration dynamics is important for low-temperature memory devices⁴⁴ that rely on topological metastability, in which quantum domain melting processes functionally limit the long-term data retention³³.

References

1. Schrödinger, E. *What is life? the physical aspect of the living cell ; with, Mind and matter ; & Autobiographical sketches.* (Cambridge University Press, 1992).
2. Turner, M. S. & Wilczek, F. Is our vacuum metastable? *Nature* **298**, 633–634 (1982).
3. Stojchevska, L. *et al.* Ultrafast switching to a stable hidden quantum state in an electronic crystal. *Science* **344**, 177–180 (2014).
4. Kibble, T. W. B. Topology of cosmic domains and strings. *J. Phys. Math. Gen.* **9**, 1387–1398 (1976).
5. Zurek, W. H. Cosmological experiments in superfluid helium? *Nature* **317**, 505–508 (1985).
6. Monaco, R., Mygind, J., Aaroe, M., Rivers, R. J. & Koshelets, V. P. Zurek-Kibble Mechanism for the Spontaneous Vortex Formation in Nb – Al / Al ox / Nb Josephson Tunnel Junctions: New Theory and Experiment. *Phys. Rev. Lett.* **96**, 180604 (2006).
7. Pitaevskii. *Physical Kinetics.* (Butterworth-Heinemann, 1981).
8. Baldan, A. Review Progress in Ostwald ripening theories and their applications to nickel-base superalloys Part I: Ostwald ripening theories. *J. Mater. Sci.* **37**, 2171–2202 (2002).
9. Kosterlitz, J. M. & Thouless, D. J. Ordering, metastability and phase transitions in two-dimensional systems. *J. Phys. C Solid State Phys.* **6**, 1181–1203 (1973).
10. Gerasimenko, Y. A. *et al.* Quantum jamming transition to a correlated electron glass in 1T-TaS₂. *Nat. Mater.* **18**, 1078–1083 (2019).
11. Lifshitz, I. M. & Kagan, Yu. Quantum Kinetics of Phase Transitions at Temperatures Close to Absolute Zero. *Sov. Phys. JETP* **35**, (1972).
12. Leggett, A. J. *et al.* Dynamics of the dissipative two-state system. *Rev. Mod. Phys.* **59**, 1–85 (1987).
13. Pospelov, M. & Pradler, J. Big Bang Nucleosynthesis as a Probe of New Physics. *Annu. Rev. Nucl. Part. Sci.* **60**, 539–568 (2010).

14. Budden, M. *et al.* Evidence for metastable photo-induced superconductivity in K3C60. *Nat. Phys.* **17**, 611–618 (2021).
15. Mraz, A. *et al.* Charge Configuration Memory Devices: Energy Efficiency and Switching Speed. *Nano Lett.* **22**, 4814–4821 (2022).
16. Villain, J. & Bak, P. Two-dimensional ising model with competing interactions : floating phase, walls and dislocations. *J. Phys.* **42**, 657–668 (1981).
17. Villain, J. Commensurate-incommensurate transition of krypton monolayers on graphite: A low temperature theory. *Surf. Sci.* **97**, 219–242 (1980).
18. McMillan, W. L. Theory of discommensurations and the commensurate-incommensurate charge-density-wave phase transition. *Phys. Rev. B* **14**, 1496–1502 (1976).
19. Park, J. W., Lee, J. & Yeom, H. W. Zoology of domain walls in quasi-2D correlated charge density wave of 1T-TaS2. *Npj Quantum Mater.* **6**, 32 (2021).
20. Meng, Z. *et al.* Atomic Bose–Einstein condensate in twisted-bilayer optical lattices. *Nature* (2023) doi:10.1038/s41586-023-05695-4.
21. Tan, W. L. *et al.* Domain-wall confinement and dynamics in a quantum simulator. *Nat. Phys.* **17**, 742–747 (2021).
22. Feynman, R. P. Simulating physics with computers. *Int. J. Theor. Phys.* **21**, 467–488 (1982).
23. Wigner, E. On the Interaction of Electrons in Metals. *Phys. Rev.* **46**, 1002–1011 (1934).
24. Alexandrov, A. S. & Mott, N. F. *Polarons & bipolarons*. (World Scientific, 1995).
25. Fazekas, P. & Tosatti, E. Electrical, structural and magnetic properties of pure and doped 1T-TaS 2. *Philos. Mag. B* **39**, 229–244 (1979).
26. Bozin, E. S. *et al.* High-temperature polaronic lattice distortions and charge ordering through the charge-density wave and quantum spin liquid phase transitions in 1T-TaS₂. Preprint at <https://doi.org/10.48550/arXiv.2301.05670> (2023).

27. Vodeb, J. *et al.* Configurational electronic states in layered transition metal dichalcogenides. *New J. Phys.* **21**, 083001 (2019).
28. Ravnik, J. *et al.* A time-domain phase diagram of metastable states in a charge ordered quantum material. *Nat. Commun.* **12**, 2323 (2021).
29. Gerasimenko, Y. A., Karpov, P., Vaskivskyi, I., Brazovskii, S. & Mihailovic, D. Intertwined chiral charge orders and topological stabilization of the light-induced state of a prototypical transition metal dichalcogenide. *Npj Quantum Mater.* **4**, 32 (2019).
30. Kranjec, A. *et al.* Electronic Dislocation Dynamics in Metastable Wigner Crystal States. *Symmetry* **14**, 926 (2022).
31. Ma, L. *et al.* A metallic mosaic phase and the origin of Mott-insulating state in 1T-TaS₂. *Nat. Commun.* **7**, 10956 (2016).
32. Cho, D. *et al.* Nanoscale manipulation of the Mott insulating state coupled to charge order in 1T-TaS₂. *Nat. Commun.* **7**, 10453 (2016).
33. Vaskivskyi, I. *et al.* Controlling the metal-to-insulator relaxation of the metastable hidden quantum state in 1T-TaS₂. *Sci. Adv.* **1**, e1500168 (2015).
34. Laulhé, C. *et al.* Ultrafast Formation of a Charge Density Wave State in 1 T – TaS₂ : Observation at Nanometer Scales Using Time-Resolved X-Ray Diffraction. *Phys. Rev. Lett.* **118**, 247401 (2017).
35. Salgado, R. *et al.* Low-frequency noise spectroscopy of charge-density-wave phase transitions in vertical quasi-2D 1T-TaS₂ devices. *Appl. Phys. Express* **12**, 037001 (2019).
36. Grabert, H., Olschowski, P. & Weiss, U. Quantum decay rates for dissipative systems at finite temperatures. *Phys. Rev. B* **36**, 1931–1951 (1987).
37. Brence, J. *et al.* Boosting the performance of quantum annealers using machine learning. *Quantum Mach. Intell.* **5**, 4 (2023).

38. Whiticar, A. M. *et al.* Probing flux and charge noise with macroscopic resonant tunneling. *Phys. Rev. B* **107**, 075412 (2023).
39. QPU-Specific Characteristics — D-Wave System Documentation documentation. https://docs.dwavesys.com/docs/latest/doc_physical_properties.html#doc-qpu-characteristics.
40. Kustov, S., Liubimova, I. & Salje, E. K. H. Domain Dynamics in Quantum-Paraelectric SrTiO 3. *Phys. Rev. Lett.* **124**, 016801 (2020).
41. Coleman, S. Fate of the false vacuum: Semiclassical theory. *Phys. Rev. D* **15**, 2929–2936 (1977).
42. Linde, A. Inflationary Cosmology. in *Inflationary Cosmology* (eds. Lemoine, M., Martin, J. & Peter, P.) vol. 738 1–54 (Springer Berlin Heidelberg, 2008).
43. Ng, K. L., Opanchuk, B., Thenabadu, M., Reid, M. & Drummond, P. D. Fate of the False Vacuum: Finite Temperature, Entropy, and Topological Phase in Quantum Simulations of the Early Universe. *PRX Quantum* **2**, 010350 (2021).
44. Vaskivskyi, I. *et al.* Fast electronic resistance switching involving hidden charge density wave states. *Nat. Commun.* **7**, 11442 (2016).

Figures

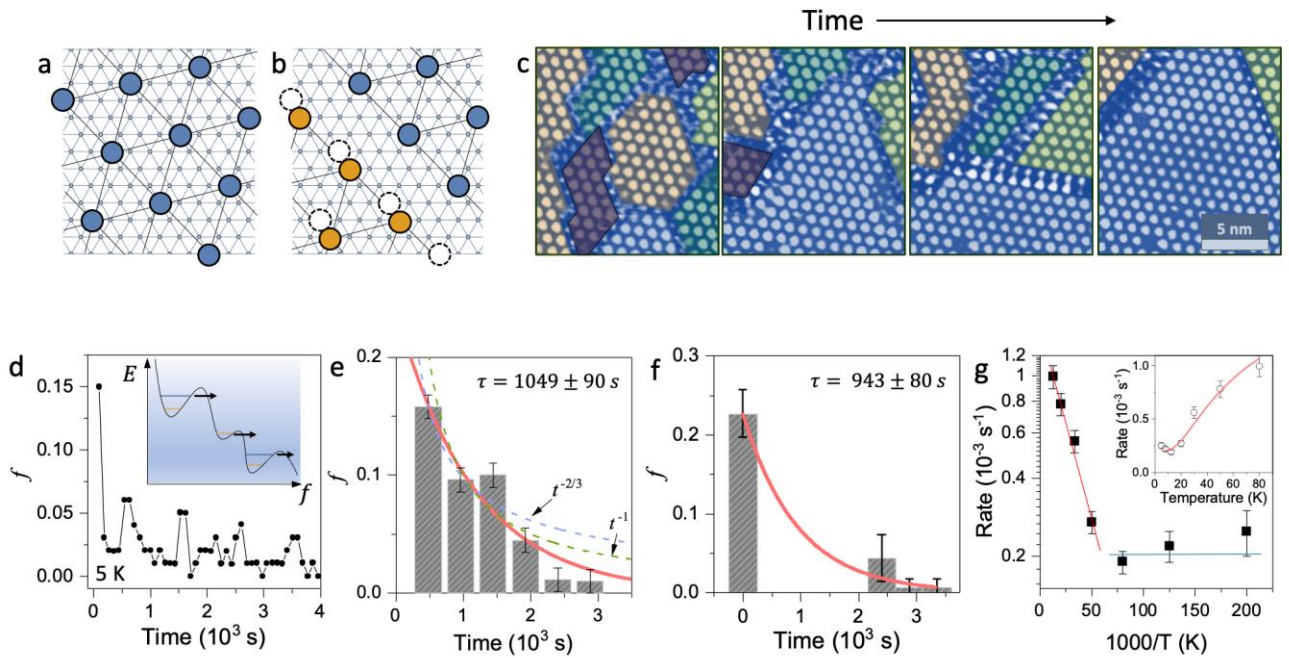


Figure 1. Domain reconfigurations in 1T-TaS₂. **a)** The crystal lattice showing Ta atoms (small circles). Occupied electron sites (blue and orange circles) **a)** in the ground state, and **b)** near a domain wall. **c)** A series of STM measurements at regular time intervals showing domain reconfiguration. Domains are colored to signify a displacement relative to the main commensurate lattice (light blue). (STM parameters: -0.8 V, 50 pA). **d)** The fraction of electrons moved $f(t)$ as a function of time measured within the same area at **5 K**. The jumps correspond to large (observable) configurational changes. The inset shows a schematic of the configurational free energy E as a function of configurational coordinate (Hamming distance) f . The excited states within each well represent states which conserve f (see text). **e)** $f(t)$ averaged over different areas of the sample, with periodic STM scans. Exponential and power law fits to the data are shown (solid and dashed lines respectively). Error bars represent counting errors. **f)** Same as **e**), except with a 32-minute gap in scanning the first point. The exponential fit is the red line. **g)** The temperature dependence of R averaged over a large number of decays on a logarithmic scale with the inset showing a linear scale.

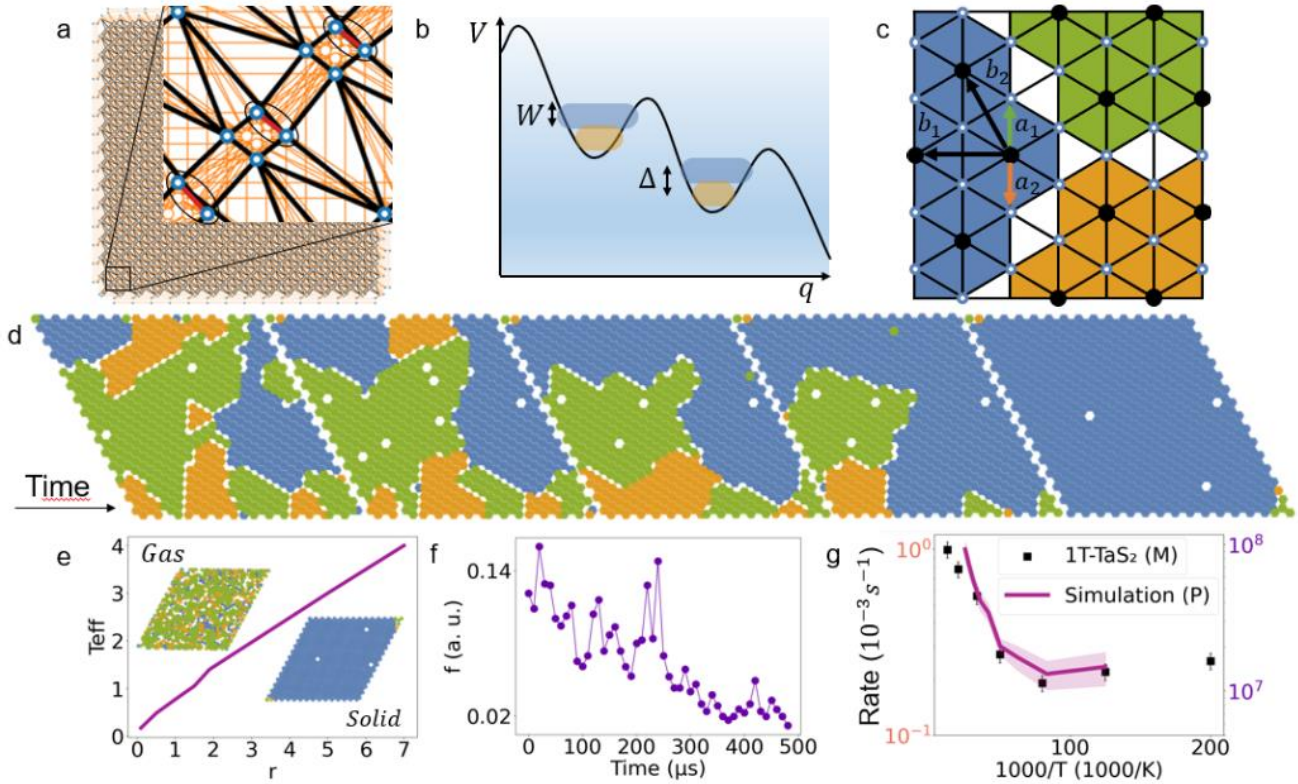


Figure 2. Simulation of emergent quantum decay based on microscopic quantum simulations.

a) Embedding of the triangular lattice used in our simulations on P with the inset showing the detailed connections between qubits. The white dots encircled with blue represent individual atomic sites (also in c)), black lines are connections between qubits we used for the nearest neighbor (NN) repulsion, red lines are physical connections used for creating logical qubits (also encircled in black) on a triangular lattice and the orange lines are the unused physical connections on the processor. **b)** The washboard potential of the NSQS flux qubit with 2-level system spacing Δ coupled to the external bath of bandwidth W . **c)** The three possible ground states of the NN repulsion we deployed on the quantum annealer. They are a $1/3$ polaronic lattice with primitive vectors \mathbf{b}_1 and \mathbf{b}_2 , shifted by two possible atomic lattice vectors \mathbf{a}_1 and \mathbf{a}_2 . The different superlattices are colored for clarity. **d)** An example of a relaxation sequence with parameters $t_a = 5 \mu\text{s}$, $r = 9$ and $T_{\text{eff}} = 1.33$. **e)** The phase diagram of our model for 1T-TaS₂ as a function of r . **f)** The Hamming distance $f(t)$ sampled from the quantum annealer for the sequence shown in d). This can be compared with experimental data in Fig. 1d). **g)** $R(T)$ extracted from the quantum annealer (P) with parameters $t_a = 5 \mu\text{s}$ and $r = 15$, and 1T-TaS₂ (M). The temperature scale for P was chosen to be $T = T_{\text{eff}} * 4K$, for demonstration purposes. See main text for actual parameter estimation.

Acknowledgments

We wish to acknowledge discussions with Tomaž Prosen, Marko Žnidarič, Andrew King and Tomaž Mertelj. Single crystals were grown for this work by Petra Sutar, funding from ARRS project P-0040, N1-0092 and young researcher grants, P17589 and P08333. This project has received funding from the European Union's Horizon 2020 research and innovation program under the Marie Skłodowska-Curie grant agreement No 701647.

Author Contributions

Michele Diego, Yevhenii Vaskivskyi, Yaroslav Gerasimenko and Dragan Mihailovic performed experimental measurements and analysis of experimental data. Jaka Vodeb conceptualized and performed quantum simulations on D-Wave's quantum annealer. Leonard Logaric and Viktor Kabanov performed theoretical analysis of data from experiment and simulation. Benjamin Lipovsek and Marko Topic performed simulations of Joule heating from the STM tip. Jaka Vodeb and Dragan Mihailovic wrote the paper. All authors contributed to the supplementary information.

Competing Interest Declaration

The authors declare no competing interests.

Supplementary Information

Supplementary Information is available for this paper.

Corresponding author

Correspondence and requests for materials should be addressed to Jaka Vodeb (jaka.vodeb@ijs.si).